Robust Bicontinuous Metal-Elastomer Foam Composites with Highly Tunable Stiffness

*Siavash Sharifi, Amir Mohammadi Nasab, Pei-En Chen, Yiliang Liao, Yang Jiao, and Wanliang Shan**

* Corresponding author.

Siavash Sharifi and Prof. Wanliang Shan
Shan Research Group, Department of Mechanical and Aerospace Engineering, Syracuse University, Syracuse, NY 13244, USA
E-mail: washan@syr.edu

Siavash Sharifi, Amir Mohammadi Nasab and Prof. Wanliang Shan
Shan Research Group, Mechanical Engineering Department, University of Nevada, Reno, NV 89557, USA

Amir Mohammadi Nasab
School of Engineering and Applied Science, Yale University, New Haven, CT 06511, USA

Pei-En Chen and Prof. Yang Jiao
Materials Science and Engineering, Department of Physics, Arizona State University, Tempe, AZ 85287, USA

Prof. Yiliang Liao
Department of Industrial and Manufacturing Systems Engineering, Iowa State University, Ames, IA, 50011, USA

Keywords: Smart Materials, LMPA Foam, Elastomer, Tunable Stiffness, Soft Robotics

Abstract:

In this paper, we propose, fabricate, characterize, and demonstrate a new class of robust bicontinuous elastomer-metal foam composites with highly tunable mechanical stiffness. The smart composite is a bicontinuous network of two foams, one metallic made of a Low Melting Point Alloy (LMPA), and the other elastomeric made of polydimethylsiloxane (PDMS). The stiffness of the composite can be tuned by inducing phase changes in its LMPA component. Below the melting point of the LMPA, Young's modulus of the smart composites is ~1 GPa, whereas above the melting point of the LMPA it is ~1 MPa. Thus, a sharp stiffness change of ~1000× can be realized through the proposed bicontinuous foam composite structure, which is higher than all available robust smart composites. We also used effective medium theory to

predict the Young's modulus of the bicontinuous smart composites, which generates reasonable agreement with experimentally measured Young's modulus of the smart composites. In the end we also demonstrate the use of these smart materials as a smart joint in a robotic arm.

Main Text:

Composite materials with tunable stiffness are mechanically stiff under one set of conditions and soft under another (e.g., when applying a voltage). These smart composites have many practical applications as artificial muscles and actuators in robotics [1–17] and wearable assistive devices [18–23]. Dynamically tunable reversible stiffness enables the robots to actively change their shapes and elastic deformations to adapt to complex environments and realize their functionalities [6,23,24]. For example, smart composites with tunable stiffness have enabled novel design of smart adhesives with dynamically tunable dry adhesion [6], which can be used as compliant grippers for pick-and-place manufacturing and transfer printing of semiconductors [23], as well as locomotion mechanisms for climbing robots [24].

Existing approaches to tunable stiffness can be roughly grouped into two categories: changing shape/geometry and altering material properties [15]. The second category typically involves using active materials such as piezoelectric materials, and adaptive (semi-active) materials such as shape memory polymers (SMP) and shape memory alloys (SMA), which have low energy requirements for activation [25–28]. There have been many studies that use adaptive materials to achieve stiffness tuning [29–44]. For example, Varga et al. [44] distributed carbonyl iron particles into a polymer network to realize such composites. When exposed to an external magnetic field, the carbonyl iron particles form a chain-like structure parallel to the magnetic field direction, leading to the increased elastic modulus of the composites. Recently, many have taken advantage of the phase change of Low Melting Point Alloys (LMPA) to reversibly tune the elastic rigidity of the elastomeric composite containing LMPA layers [31], particles [34], and foams [33]. In one such study, an elastomer foam is infiltrated with melted LMPA to form a foam

composite, whose Young's modulus can be reduced by 18 times when externally heated above the LMPA's melting point [33].

However, these recent instances of smart composite materials with tunable mechanical stiffness still suffer from critical drawbacks. For example, there is an insufficient change in mechanical stiffness due to the fact that stiffness variation results from glass transition of the elastomer co-polymer matrix [32] or lack of connectivity in the LMPA component [33], neither of which allows the composites to be rigid enough in the non-activated state. In addition, there are robustness and reversibility issues. For example, for the multilayer composite containing an LMPA layer for rigidity tuning [31], it is a heterogeneous structure rather than a homogenous material, which makes it hard to return to its original shape after large deformation. Thus, there exists a need for novel composite materials with improved tunable properties and improved robustness.

In this paper, we address these limitations by proposing and demonstrating a robust bicontinuous elastomer-LMPA foam composites with highly tunable mechanical stiffness (**Figure 1**). The composite material is a bicontinuous network of two foams, one metallic, made of LMPA, and the other elastomeric, made of polydimethylsiloxane (PDMS). The stiffness of the composite can be tuned by inducing phase changes in its LMPA component. The LMPA used in this study is Cerrolow 117 (composition by weight: 45% bismuth, 23% lead, 19% indium, 8% tin, and 5% cadmium), which melts at 47.2 °C. Below 47.2 °C, the composite is stiff and behaves like a solid metal. Above 47.2 °C, Cerrolow 117 becomes liquid, therefore the mechanical properties of the polymer foam dominate the composite's mechanical properties. Cerrolow 117 has a high elastic modulus of ≅ 8.5 GPa at room temperature (obtained using tensile tests on three standard samples in this study), while PDMS has an elastic modulus of ≅ 2 MPa [31]. Taking advantage of the mechanical properties of both materials makes possible the wide range of stiffness tuning and shape morphing. A sharp stiffness change of ~1000× can be realized through the proposed bicontinuous foam composites, which is higher than most of the

aforementioned previous studies, except for the multilayered one with robustness issue [31]. The optical images of the LMPA foam and the bicontinuous composite made of the LMPA foam infiltrated by PDMS, as well as a schematic of the bicontinuous smart composite are shown in **Figure 1 (a-d)**. Improved robustness of this novel smart material compared with previously reported ones can be inferred from the more homogenous distribution of the LMPA phase inside the composite. A composite beam in both activated and non-activated status with different deflections are compared in **Figure 1 (e-g)**. The activation time is affected by the heating power of the heat gun used, while deactivation can be faster if active cooling is adopted. The deflection of a PDMS beam with the same geometry as the composite one under the same load is shown in **Figure 1** (h, i). As can be observed, the smart composite in the non-activated state is much stiffer than the pure PDMS as its deflection is much lower under the same load. Additionally, the activated smart composite is even softer than the pure PDMS beam with the same geometry as the deflections indicate.

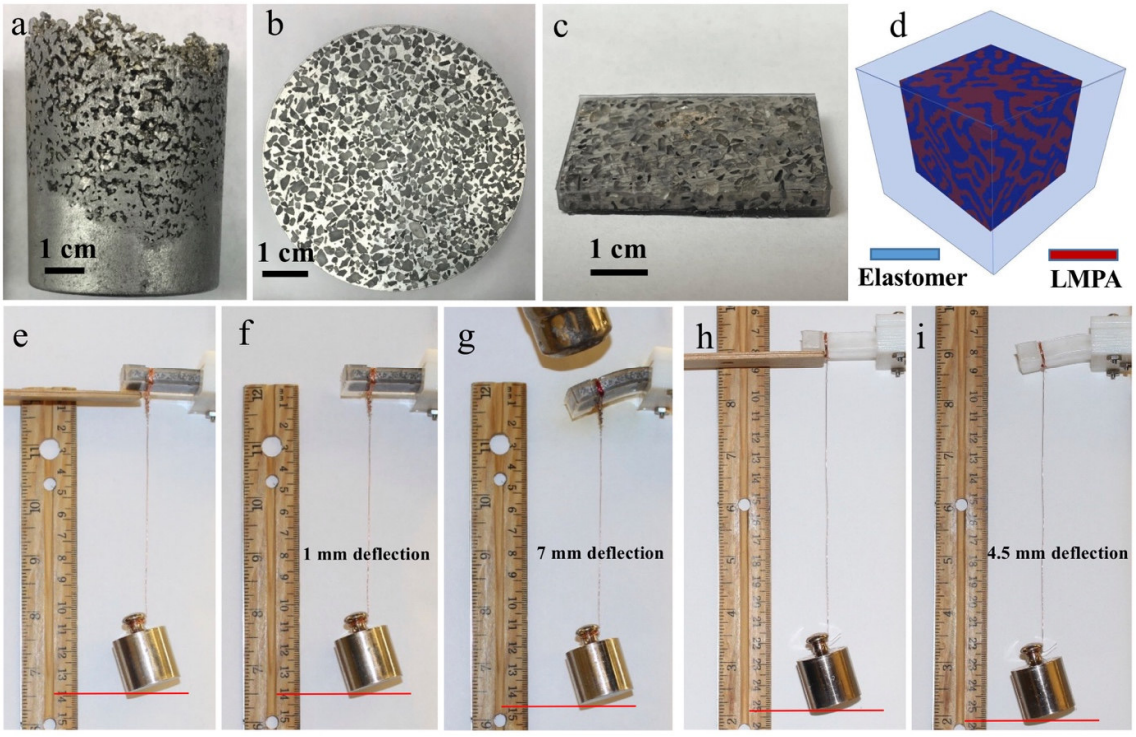

Figure 1. a) Side view of the metal foam. b) top view of a metal foam slice. c) A rectangular-shaped smart composite sample containing an LMPA foam infiltrated by a PDMS matrix. d) Schematic of the bicontinuous elastomer-LMPA smart composite wrapped around by an external layer of elastomer. e) a non-activated

composite beam with no dead weight applied. f) a non-activated composite beam with 100 g dead weight applied on its free end. g) an activated composite beam with 100 g dead weight applied on its free end. h) a PDMS beam of the same dimensions as the smart composite beam in panels d-f with no dead weight applied. i) The PDMS beam in panel g with 100 g dead weight applied on its free end.

To fabricate this bicontinuous composite, an LMPA foam containing a well-connected network of pores is formed first. Here, we used a replication procedure that has been used to make open-cell aluminum foams [45–47] to prepare the LMPA foam. The experimental setup is illustrated in **Figure 2 (a)**. A step-by-step procedure of LMPA foam fabrication is shown in **Figure 2 (b)**. The first step is pouring the table salt particles into the mold cylinder, followed by placing the prepared metal on top of the salt particles. After that, the lid of the mold is sealed with a soft washer. At this stage, the top of the lid is attached to the valve system, and all valves of the system are closed. Next, the mold is placed on a hot plate set to 86 °C. The valve connecting the vacuum pump with the mold is then opened and left open for about two hours. Next, all the valves of the system are closed. The main valve of the argon gas tank is then opened, and the infiltration pressure is set with the regulator valve (≈120 psi). The valve of argon gas is left open until the mold completely cools. Pressurized argon gas is used here to drive the melted LMPA into the salt particles, because the melted LMPA doesn't wet the salt, which is a common phenomenon for most molten metals in contact with ionic solids [46]. Next, the valve system is detached, and the mold lid is removed. The salt-LMPA foam is taken out from the mold and cut using a saw. Finally, the salt-LMPA foam is placed in a beaker with water and a magnetic stirring bar on a stirring plate to dissolve the salt particles. The next step is to fill the pores of the LMPA foam with PDMS by embedding the foam into a 3d-printed mold, casting uncured PDMS into the mold, and then curing the PDMS. In addition, at this stage, a thin layer of PDMS (~1 mm thick) is added around the LPMA foam to prevent leaking the LPMA when it's in the liquid state. The final smart composite is shown in **Figure 1 (c)**.

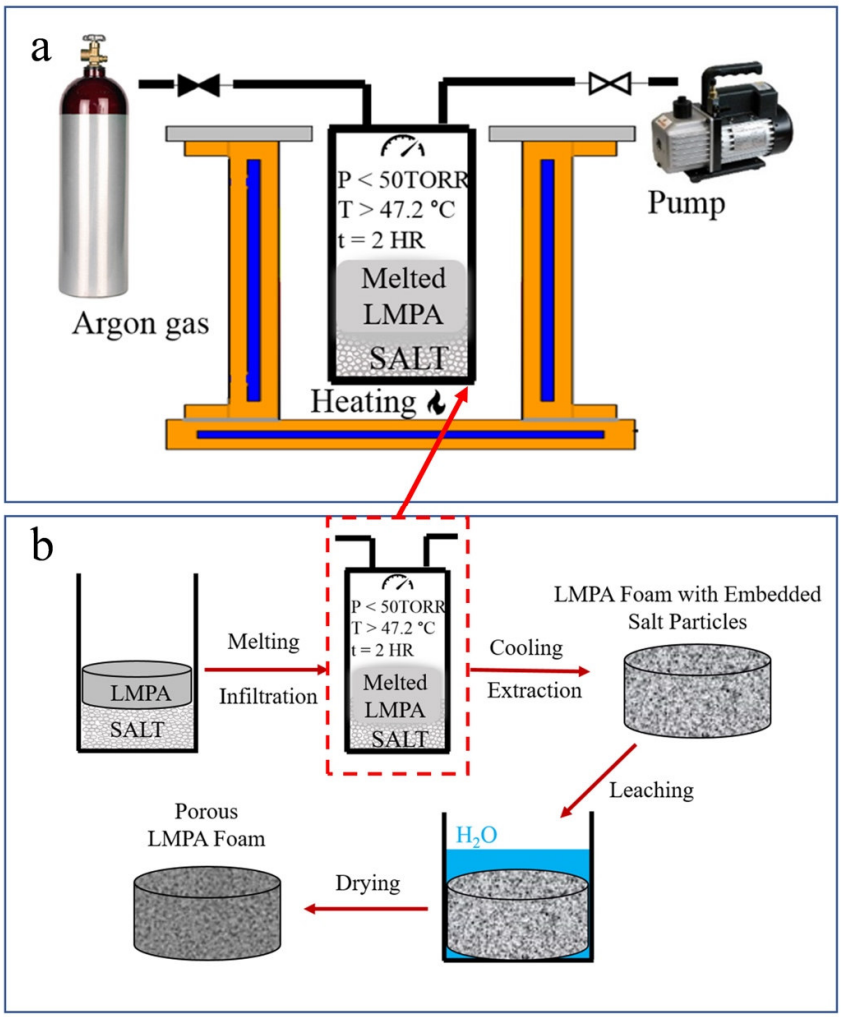

Figure 2. a) The experimental setup, and b) the fabrication procedures for the LMPA foam.

The stress-strain behaviors of the fabricated smart composites are systematically characterized. These smart materials are rigid at temperatures below the melting point of Cerrolow 117 (47.2 °C) and thus are able to hold an external load at room temperature without much deflection as shown in **Figure 1 (e)**. Since the smart composite is highly electrically conductive and cannot be directly heated through Joule heating, a heat gun is used to activate them. For the nonactivated case, 9 different smart composite samples with the geometry of (37.96 ± 1.107) * (20.22 ± 0.212) * (3.06 ± 0.495) mm^3 are used to measure the Young's modulus. The composite sample surfaces are polished to remove excess PDMS that can jeopardize firm clamping. Using a direct method (see **Experimental Section** for more details), the porosities of these composite samples are measured to be from 20% to 63% (SI, Table S3). **Figure 1 (c)** is an optical image

of one of these composite samples, and **Figure 3 (a)** illustrates a typical stress-strain curve of these composite samples. The slope of the initial linear part of Figure 3b is used to calculate the Young's modulus of these composites. **Figure 3(b)** shows how the measured Young's modulus of the 9 composite samples at room temperature changes with the porosity measured using experiments, whereas the bar plot in Figure 3(c) presents the same data using sample number as the x-axis. More details about the results can be found in Supporting Information.

To put in context of the experimental measurements, we have calculated the upper and lower bounds of the Young's moduli for these composite samples using rule of mixtures and the tighter Hashin–Shtrikman bounds [48] (SI, Table S1 and S2) and included these in the log plot in **Figure 3 (b)**. As shown, although Hashin-Shtrikman bounds are indeed better than those based on the rule of mixture, they are still too crude to estimate the modulus of the bicontinuous smart composite materials. A better modeling approach is needed.

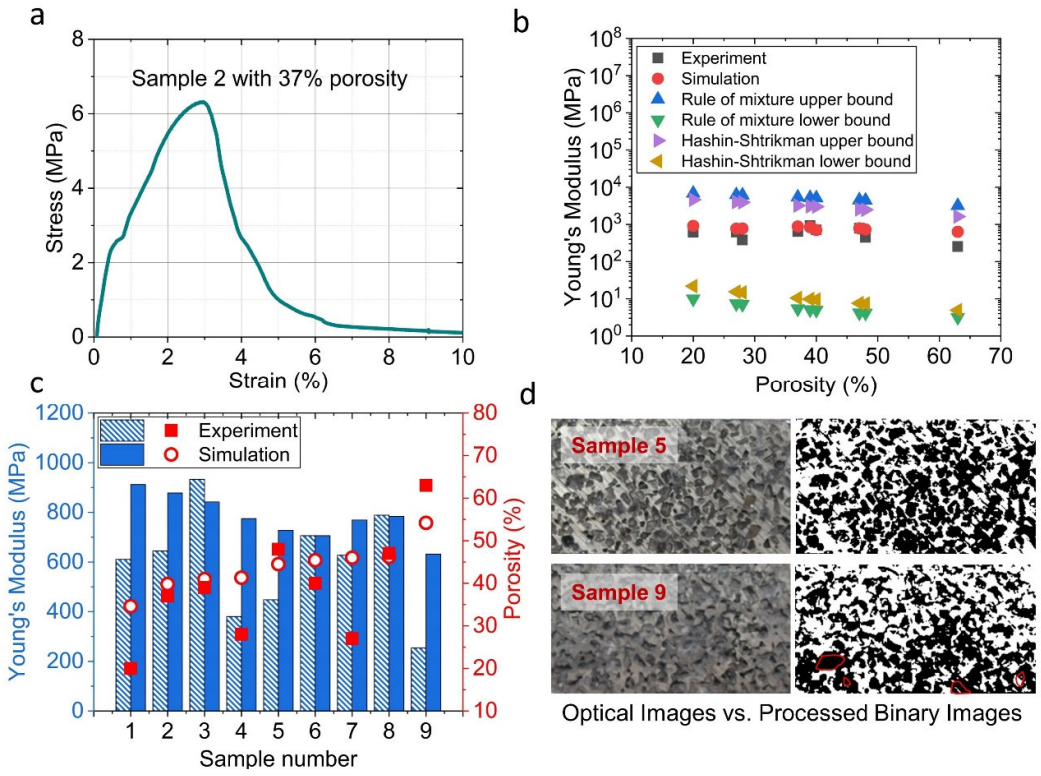

Figure 3. a) A typical stress-strain curve of the smart composite. b) Young's modulus values from experiments and simulation compared to the upper and lower bounds based on the Hashin–Shtrikman model and rule of

mixtures. c) Comparison of porosities and Young's modulus obtained from experiments and simulation for each smart composite sample. d) Optical (left) and processed binary (right) images of smart composite samples.

Effective-medium theory (EMT) is thus used to estimate the Young's modulus of the smart composites by explicitly considering the microstructure of the smart composites, including both volume fractions and their high-order spatial correlations obtained from optical images of the cross-sections of the smart composites. In particular, we employ the strong-contrast formalism developed by Torquato [49], which allows one to express the elastic moduli of a heterogeneous material as a series of integrals involving the individual phase properties and correlation functions S_n [50] . These correlation functions provide the probability of finding a specific n-point configuration in the phase of interest in the material. Truncating the series at lower-order n allows one to derive approximations of the effective moduli. Here S_n and other microstructural parameters involving integrals of S_n are computed directly from 2D imaging data, assuming that the material is statistically homogeneous and isotropic such that the structural statistics and spatial correlation functions computated from a 2D slice of the material are representative of the actual 3D microstructure. More details about this procedure can be found in Supporting Information.

Figure 3 (d) shows a side-by-side comparison between two optical images (left) of the sample surfaces and the corresponding processed binary plots (right) that are used for extraction of microstructure information of the smart composites, including porosity and other higher-order microstructural parameters**. Figures 3 (d)** indicate that for sample number 5 the optical image and the processed binary plot are in good match, whereas for sample number 9 there are certain areas in the binary plot that are not accurately reflecting what is in the optical image, which is attributed to the low contrast of these regions in the optical image. These artifacts could lead to inaccuracy of the computed higher-order structural parameters, and thus, the estimated modulus. Another possible source of inaccuracy involves the violation of the assumption of statistical

homogeneity and isotropy of the material systems. Nevertheless, it can be seen in **Figure 3 (b)** that the proposed modeling method gives estimations on the same order as those experimental values, much better when compared to those from Hashin–Shtrikman model and rule of mixture. Note that here in **Figure 3 (b)**, the porosity data from experiments are used for the samples to allow for easy comparison of Young's modulus values. **Figure 3 (c)** shows the comparison of porosities and Young's modulus measured from experiments for each sample along with those obtained through simulation. The sample is numbered in a way such that their simulated porosity is increasing (see Supporting Information for details). In general, both the experiments and simulation data show a decreasing Young's modulus with increasing porosity. The differences in Young's modulus between the measured ones and simulated ones (maximum difference ~60%) are much smaller than those predictions by rule of mixture and Hashin–Shtrikman model, indicating good agreement between experiments and EMT modeling. We note that sample 6 and sample 8 have 45.4% and 46.2% porosity from modeling, with the elastic moduli of 706 MPa and 784 MPa, respectively. Porosity is not the only parameter that affects elastic modulus, in fact the structure of the sample has some effects too. The SCE method used here also incorporated higher-order structural parameters depending on 3-pt correlations of the phase, which were computed from the segmented 2D images. Although sample 8 possesses a slightly higher porosity, it also exhibits large regions of percolating metal phase, which could have led to the slightly higher modulus.

We also experimentally measured the Young's modulus of the smart composites in the activated case. Three tests have been performed on each of the three samples with experimentally measured porosity 25%, 32%, and 38%, and corresponding Young's modulus are tested to be 0.548 ± 0.01 MPa, 0.633 ± 0.12 MPa, and 2.3 ± 0.01 MPa, respectively. More details can be found in Supporting Information Table S4. EMT modeling was also conducted for these three activated samples to estimate their Young's modulus at nonactivated status, which were

predicted to be 908.2 MPa, 748.5 MPa, 833.6 MPa, respectively (SI Table S4). These translate to stiffness changes of 1657, 1182, and 362 times, respectively. It is thus deduced that these smart composites can exhibit stiffness changes of three orders of magnitude, and that typically lower porosity of the LMPA foam will result in higher stiffness change of the bicontinuous composite.

In addition, due to the elastomer matrix of the smart composites, these smart materials also have shape memory effects. Both shape fixity and shape recovery are characterized for these smart composites. Shape fixity, R_f, is the extent to which a temporary shape can be preserved for a material after load removal, while shape recovery, R_r, is the ability of the material to return to the original shape after being held in a temporary shape for some time. $R_f = \varepsilon/\varepsilon_{load}$, where ε is the temporary strain after load removal and ε_{load} is the initial applied strain at the soft state. $R_r = (\varepsilon - \varepsilon_{recovery})/\varepsilon$, where $\varepsilon_{recovery}$ is the permanent strain after shape recovery. The shape fixity and shape recovery of these smart composites are measured to be 83.6% ± 1.24% and 97.6% ± 0.35%, respectively, based on yet another three samples tested. These values attest to the robustness of these smart composites.

These robust smart composites with sharp stiffness change and shape memory effect can be used in many soft robotic applications, especially where heavy-lifting is involved. Here we demonstrate this by designing a robotic arm containing smart joints made of the novel smart composites. The smart composite joint consists of a block of the smart composite, a 3d printed frame and a flexible rope heater wrapped around the smart composite. The flexible rope heater was used to activate the smart composite. The robotic arm has one degree of freedom, which can be modulated using a tendon attached to a servomotor. The smart joint allows the robotic arm to bend in one direction when it is activated. In the non-activated case, it is rigid and is able to hold heavy weights; however, it behaves like a soft material when activated and is able to bend, as demonstrated in **Figure 4**.

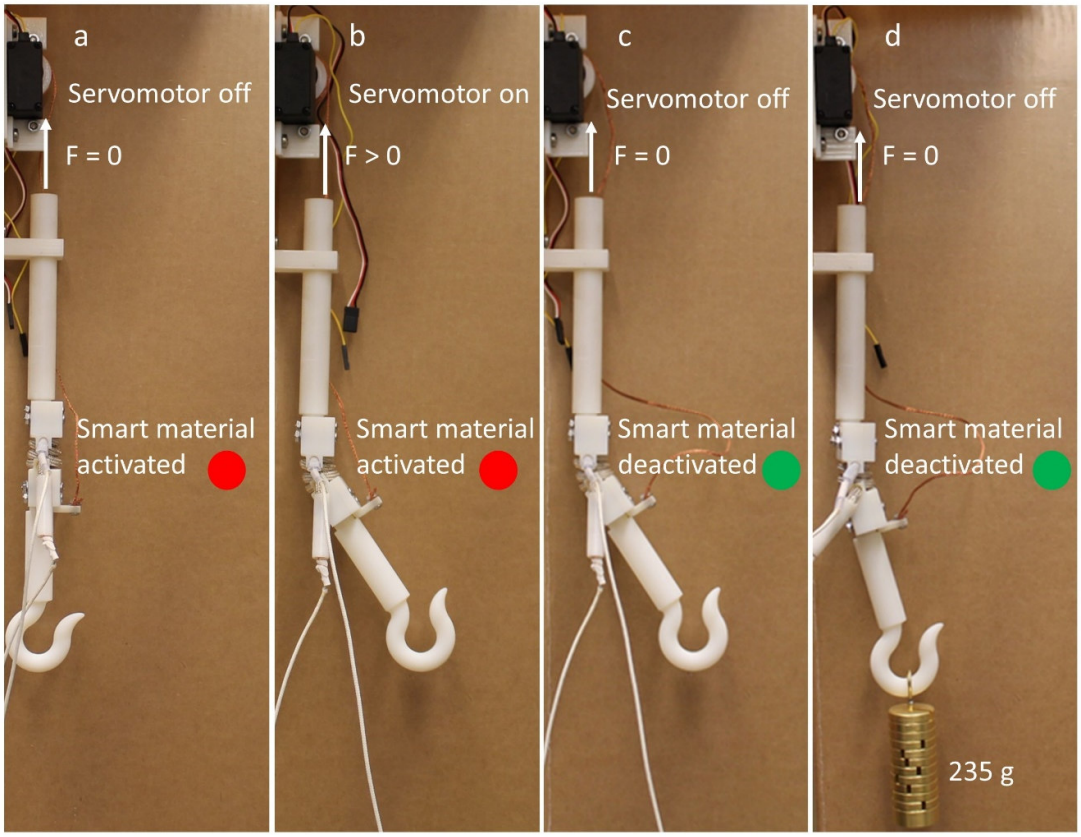

Figure 4. Robotic arm made with the smart composite. (a) the robotic arm without any force applied. (b) After activation through a flexible rope heater, it can easily bend by the servomotor. (c, d) After cooling down, the arm can retain its shape while holding weights. Note that the compliance of the 3d-printed arms contributed to much of the reduction of the bending angle of the joint here.

In conclusion, smart composites with tunable stiffness of three orders of magnitude have been manufactured by infiltrating an elastomer matrix into an open-connected LMPA foam. The composite is rigid at room temperature with a Young's modulus ~ 1 GPa, and it becomes soft at temperatures above the LMPA's melting point (47 °C) with a Young's modulus ~ 1MPa. The fabrication of these smart composites involves replication and infiltration, and the mechanical properties of the smart composite before and after activation are characterized systematically using experiments. Moreover, the effective medium theory is used to estimate the Young's modulus of the smart composites, which agrees well with experimental results. The smart composites also have shape memory effect due to their elastomeric matrix, which is

characterized experimentally. Towards the end, we demonstrate the use of these smart composites as smart joints in a robotic arm lifting weights.

Experimental Section

Mechanical Testing:

A motorized tensile test machine (Instron 6959) was used to measure the Young's modulus of the smart composites. Given the difficulty in directly clamping elastomeric materials, we removed the sealing PDMS layer on the smart composite surface using sandpapers for the non-activated cases such that slipping between the sample surface and the clamping fixture was minimized. For activated cases, a piece of fabric was used to make the grip easier. The Young's modulus value was obtained by calculating the slope of the initial straight portion of the stress-strain curves (**Figure 3(a)**).

Foam Porosity Measurements:

In order to measure the porosity of the LMPA foams, we first measured the dimensions of each foam sample and calculated its total volume assuming no pores. Then, we immersed each individual foam sample into a graduated cylinder containing water. Next, we recorded the change in the water level marked by the graduated cylinder, and took that change to be the actual volume of the LMPA in the LMPA foam sample. Finally, the difference between the total volume of the LMPA foam and the actual volume of the LMPA was calculated to be the porosity volume in the foam and its percentage is calculated accordingly.

Acknowledgements

This work was supported by a differential fee assistantship provided by University of Nevada, Reno to S. Sharifi, and start-up funds provided by Syracuse University to W. Shan. This work is also supported by National Science Foundation under awards CMMI-1830388 and DMR-2020277.

[1] L. Hines, V. Arabagi, M. Sitti, *IEEE Trans. Robot.* **2012**, *28*, 987.
[2] Y. J. Kim, S. Cheng, S. Kim, K. Iagnemma, *IEEE Trans. Robot.* **2013**, *29*, 1031.
[3] Y. Yang, Y. Chen, Y. Wei, Y. Li, *J. Mech. Robot.* **2016**, *8*, DOI 10.1115/1.4033728.
[4] Y. Zhang, N. Zhang, H. Hingorani, N. Ding, D. Wang, C. Yuan, B. Zhang, G. Gu, Q. Ge, *Adv. Funct. Mater.* **2019**, *29*, 1806698.
[5] C. Chautems, A. Tonazzini, Q. Boehler, S. H. Jeong, D. Floreano, B. J. Nelson, *Adv. Intell. Syst.* **2019**, 1900086.
[6] A. M. Nasab, A. Sabzehzar, M. Tatari, C. Majidi, W. Shan, *Soft Robot.* **2017**, *4*, 411.
[7] J. Sun, J. Zhao, *IEEE Robot. Autom. Lett.* **2019**, *4*, 724.
[8] M. Al-Rubaiai, T. Pinto, C. Qian, X. Tan, *Soft Robot.* **2019**, *6*, 318.
[9] J. Santoso, E. H. Skorina, M. Salerno, S. De Rivaz, J. Paik, C. D. Onal, *Smart Mater. Struct.* **2019**, *28*, DOI 10.1088/1361-665X/aaf9c0.
[10] K. C. Galloway, J. E. Clark, D. E. Koditschek, in *Proc. ASME Des. Eng. Tech. Conf.*, **2009**, pp. 215–222.
[11] Z. Qaiser, L. Kang, S. Johnson, *Mech. Mach. Theory* **2017**, *110*, 1.
[12] Y. She, H. J. Su, C. Lai, D. Meng, in *Proc. ASME Des. Eng. Tech. Conf.*, American Society Of Mechanical Engineers (ASME), **2016**.
[13] T. H. Yang, H. J. Kwon, S. S. Lee, J. An, J. H. Koo, S. Y. Kim, D. S. Kwon, *Sensors Actuators, A Phys.* **2010**, *163*, 180.
[14] Y. Wei, Y. Chen, Y. Yang, Y. Li, *Mechatronics* **2016**, *33*, 84.
[15] I. K. Kuder, A. F. Arrieta, W. E. Raither, P. Ermanni, *Prog. Aerosp. Sci.* **2013**, *63*, 33.
[16] E. Brown, N. Rodenberg, J. Amend, A. Mozeika, E. Steltz, M. R. Zakin, H. Lipson, H. M. Jaeger, *Proc. Natl. Acad. Sci.* **2010**, *107*, 18809.
[17] A. Shiva, A. Stilli, Y. Noh, A. Faragasso, I. De Falco, G. Gerboni, M. Cianchetti, A. Menciassi, K. Althoefer, H. A. Wurdemann, *IEEE Robot. Autom. Lett.* **2016**, *1*, 632.
[18] F. L. Hammond III, F. Wu, H. H. Asada, **2018**, pp. 201–217.
[19] H. K. Yap, J. H. Lim, F. Nasrallah, F. Z. Low, J. C. H. Goh, R. C. H. Yeow, in *IEEE Int. Conf. Rehabil. Robot.*, IEEE Computer Society, **2015**, pp. 735–740.
[20] T. P. Chenal, J. C. Case, J. Paik, R. K. Kramer, in *IEEE Int. Conf. Intell. Robot. Syst.*, Institute Of Electrical And Electronics Engineers Inc., **2014**, pp. 2827–2831.
[21] S. Hauser, M. Robertson, A. Ijspeert, J. Paik, *IEEE Robot. Autom. Lett.* **2017**, *2*, 849.
[22] S. I. Rich, V. Nambeesan, R. Khan, C. Majidi, *J. Intell. Mater. Syst. Struct.* **2019**, *30*, 2908.
[23] M. Tatari, A. Mohammadi Nasab, K. T. Turner, W. Shan, *Adv. Mater. Interfaces* **2018**, *5*, 1800321.
[24] S. Sharifi, C. Rux, N. Sparling, G. Wan, A. Mohammadi Nasab, A. Siddaiah, P. Menezes, T. Zhang, W. Shan, *Front. Robot. AI* **2021**, *8*, 191.
[25] R. D. Kornbluh, H. Prahlad, R. Pelrine, S. Stanford, M. A. Rosenthal, P. A. von Guggenberg, in *Smart Struct. Mater. 2004 Ind. Commer. Appl. Smart Struct. Technol.*, SPIE, **2004**, p. 372.
[26] S. Hurlebaus, L. Gaul, *Mech. Syst. Signal Process.* **2006**, *20*, 255.
[27] K. Makihara, J. Onoda, K. Minesugi, *J. Vib. Acoust. Trans. ASME* **2007**, *129*, 84.
[28] H. Ji, J. Qiu, P. Xi, in *Vib. Control*, Sciyo, **2010**.
[29] R. Takahashi, T. L. Sun, Y. Saruwatari, T. Kurokawa, D. R. King, J. P. Gong, *Adv. Mater.* **2018**, *30*, 1706885.
[30] T. L. Buckner, M. C. Yuen, S. Y. Kim, R. Kramer-Bottiglio, *Adv. Funct. Mater.* **2019**, *29*, 1903368.
[31] W. Shan, T. Lu, C. Majidi, *Smart Mater. Struct.* **2013**, *22*, 085005.
[32] W. Shan, S. Diller, A. Tutcuoglu, C. Majidi, *Smart Mater. Struct.* **2015**, *24*, DOI 10.1088/0964-1726/24/6/065001.

[33] I. M. Van Meerbeek, B. C. Mac Murray, J. W. Kim, S. S. Robinson, P. X. Zou, M. N. Silberstein, R. F. Shepherd, *Adv. Mater.* **2016**, *28*, 2801.
[34] A. Mohammadi Nasab, S. Sharifi, S. Chen, Y. Jiao, W. Shan, *Adv. Intell. Syst.* **2021**, *3*, 2000166.
[35] W. Shan, *Polymer Matrix Composites with Tunable Properties*, **2020**.
[36] F. Deng, Q. K. Nguyen, P. Zhang, *Addit. Manuf.* **2020**, *33*, 101117.
[37] R. Poon, J. B. Hopkins, *Adv. Eng. Mater.* **2019**, *21*, 1900802.
[38] C. Chautems, A. Tonazzini, D. Floreano, B. J. Nelson, in *IEEE Int. Conf. Intell. Robot. Syst.*, Institute Of Electrical And Electronics Engineers Inc., **2017**, pp. 181–186.
[39] Y. Hao, T. Wang, Z. Xie, W. Sun, Z. Liu, X. Fang, M. Yang, L. Wen, *J. Micromechanics Microengineering* **2018**, *28*, DOI 10.1088/1361-6439/aa9d0e.
[40] A. Tonazzini, S. Mintchev, B. Schubert, B. Mazzolai, J. Shintake, D. Floreano, *Adv. Mater.* **2016**, *28*, 10142.
[41] S. Rich, S.-H. Jang, Y.-L. Park, C. Majidi, *Adv. Mater. Technol.* **2017**, *2*, 1700179.
[42] T. L. Buckner, E. L. White, M. C. Yuen, R. A. Bilodeau, R. K. Kramer, in *IEEE Int. Conf. Intell. Robot. Syst.*, Institute Of Electrical And Electronics Engineers Inc., **2017**, pp. 3728–3733.
[43] E. A. Allen, L. D. Taylor, J. P. Swensen, *Smart Mater. Struct.* **2019**, *28*, DOI 10.1088/1361-665X/ab1ec9.
[44] Z. Varga, G. Filipcsei, M. Zrínyi, *Polymer (Guildf).* **2006**, *47*, 227.
[45] J. Banhart, *Prog. Mater. Sci.* **2001**, *46*, 559.
[46] Y. Conde, J.-F. Despois, R. Goodall, A. Marmottant, L. Salvo, C. San Marchi, A. Mortensen, *Adv. Eng. Mater.* **2006**, *8*, 795.
[47] R. Goodall, A. Mortensen, *Phys. Metall.* **2014**, 2399.
[48] Z. Hashin, S. Shtrikman, *J. Mech. Phys. Solids* **1963**, *11*, 127.
[49] D. C. Pham, S. Torquato, *J. Appl. Phys.* **2003**, *94*, 6591.
[50] S. Torquato, G. Stell, *J. Chem. Phys.* **1982**, *77*, 2071.